J-Substitution Algorithm in Magnetic Resonance Electrical Impedance Tomography (MREIT): Phantom Experiments for Static Resistivity Images

Hyun Soo Khang, Byung Il Lee, Suk Hoon Oh, Eung Je Woo*, *Member, IEEE*, Soo Yeol Lee, *Member, IEEE*, Min Hyoung Cho, *Member, IEEE*, Ohin Kwon, Jeong Rock Yoon, and Jin Keun Seo

***Abstract*—Recently, a new static resistivity image reconstruction algorithm is proposed utilizing internal current density data obtained by magnetic resonance current density imaging technique. This new imaging method is called magnetic resonance electrical impedance tomography (MREIT). The derivation and performance of J-substitution algorithm in MREIT have been reported as a new accurate and high-resolution static impedance imaging technique via computer simulation methods. In this paper, we present experimental procedures, denoising techniques, and image reconstructions using a 0.3-tesla (T) experimental MREIT system and saline phantoms. MREIT using J-substitution algorithm effectively utilizes the internal current density information resolving the problem inherent in a conventional EIT, that is, the low sensitivity of boundary measurements to any changes of internal tissue resistivity values. Resistivity images of saline phantoms show an accuracy of 6.8%–47.2% and spatial resolution of 64×64. Both of them can be significantly improved by using an MRI system with a better signal-to-noise ratio.**

***Index Terms*—Internal current density, J-substitution algorithm, magnetic resonance electrical impedance tomography (MREIT), resistivity image.**

I. Introduction

In static imaging of Electrical Impedance Tomography (EIT), we usually inject patterns of currents and measure voltage data on a set of surface electrodes to reconstruct the absolute values of a cross-sectional resistivity distribution of a subject [1], [2]. Even though dynamic imaging, where any temporal changes in resistivity distribution are imaged, has been finding different clinical applications, static imaging is still far from clinical applications. Most static resistivity image reconstruction algorithms suffer from low accuracy and spatial resolution mainly due to the inherent poor sensitivity of boundary measurements to any changes of internal tissue resistivity values [3]–[9]. Errors in modeling the irregular boundary shape of the subject and electrodes are another major problems.

Lately, Magnetic Resonance Electrical Impedance Tomography (MREIT) has been suggested to overcome the ill-posedness of static impedance imaging problem [10]–[15]. Even though MREIT requires an expensive Magnetic Resonance Imaging (MRI) system, it is very promising to reconstruct accurate cross-sectional resistivity images with a high spatial resolution.

In MREIT, magnetic resonance current density imaging (MRCDI) is performed to obtain the internal current density data. Externally injected currents during MRI distort MR phase images in such a way that the phase change is proportional to the z component of the induced magnetic flux density, B_z [16]–[21]. In this paper, z direction indicates the direction of the main magnetic field in an MRI system. Since we can measure only B_z, we must rotate the subject in order to acquire a complete set of data of the induced magnetic flux density $\boldsymbol{B} = (B_x, B_y, B_z)$. Once we get $\boldsymbol{B}$, we can compute the internal current density due to the injection current as $\boldsymbol{J} = \nabla \times \boldsymbol{B}/\mu_0$ where μ_0 is the permeability of free space and biological tissues.

Zhang proposed a resistivity image reconstruction algorithm utilizing the measurements of internal $\boldsymbol{J}$ and boundary voltage data [10]. His method is based on the relationship, $V_{1,2} = \int_l \rho \boldsymbol{J} \cdot \boldsymbol{dl}$ where $V_{1,2}$ is the voltage difference between two locations 1 and 2 at the boundary, l is an interior line integral path connecting 1 and 2, and ρ is the resistivity. After discretization of the imaging slice into M pixels, we can construct a linear system of equation $\boldsymbol{V}_{N\times 1} = \boldsymbol{G}_{N\times M}\boldsymbol{\rho}_{M\times 1} + \boldsymbol{n}_{N\times 1}$ where N is the number of boundary voltage measurements and $\boldsymbol{n}$ is a noise vector. Assuming that we measure current density at every pixel, the matrix $\boldsymbol{G}$ contains internal current density data and we can reconstruct the resistivity image $\boldsymbol{\rho}$ by solving the linear system of equation. A drawback of this method is the requirement of many boundary voltage measurements to improve the accuracy and spatial resolution of the resistivity image. Woo *et al.* [11] proposed a different method where the error between the current density measured by MRCDI technique and the current density calculated by the finite-element method (FEM) is minimized as a function of the resistivity distribution of the finite-element model. Eyuboglu *et al.* [12] also used a finite-element model with measured boundary voltages and injection current

Manuscript received August 23, 2001; revised February 22, 2002. This work was supported by the Korea Science & Engineering Foundation under Grant no. R01-2000-00385. *Asterisk indicates corresponding author.*

H. S. Khang, S. H. Oh, S. Y. Lee and M. H. Cho are with the Graduate School of East–West Medical Sciences, Kyung Hee University, Kyungki 449-701, S. Korea.

B. I. Lee is with the College of Electronics and Information, Kyung Hee University, Kyungki 449-701, S. Korea.

*E. J. Woo is with the College of Electronics and Information, Kyung Hee University, 1 Seochun, Kiheung, Yongin, Kyungki, 449-701, S. Korea (e-mail: ejwoo@khu.ac.kr).

O. Kwon is with the Department of Mathematics, Konkuk University, Korea.

J. R. Yoon is with the School of Mathematics, Korea Institute for Advanced Study, Korea.

J. K. Seo is with the Department of Mathematics, Yonsei University, Korea.

Publisher Item Identifier 10.1109/TMI.2002.800604.

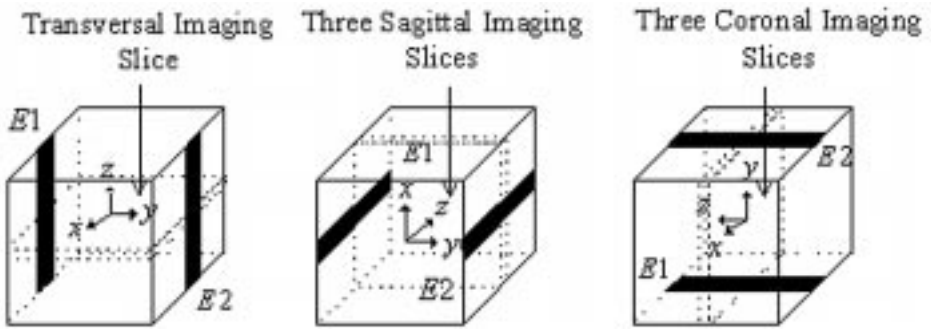

Fig. 1. Measurements of (a) B_z, (b) B_x, and (c) B_y for the injection current I between electrodes $E1$ and $E2$.

as boundary conditions. Their method is iterative assuming an initial guess on the resistivity distribution. For a given resistivity distribution of the model, they computed internal current density using FEM and updated the resistivity distribution to minimize the error between this current density and the measured one by MRCDI technique.

Lately, Kwon *et al*. developed a new resistivity image reconstruction technique called J-substitution algorithm in MREIT [13]–[15]. The final form of the algorithm is simple and intuitive using the internal current density information in an efficient way. From computer simulations, they showed that the spatial resolution of the reconstructed resistivity images is comparable with that of MR images. They also showed that the accuracy of the reconstructed resistivity values is limited by the amount of noise in the current density data. In this paper, we present experimental procedures, denoising techniques, and image reconstructions using a 0.3-tesla (T) experimental MREIT system and saline phantoms. We also describe the factors affecting the performance of J-substitution algorithm in MREIT.

II. Methods

A. MRCDI Technique

Since MRCDI technique is well known by [16]–[21], we briefly describe how we measure the induced magnetic flux density $\boldsymbol{B}$ due to an injection current. Fig. 1 shows a cubic subject Ω with two electrodes $E1$ and $E2$ attached on the boundary $\partial\Omega$. We inject a current I into the subject Ω through $E1$ and $E2$. Let $\boldsymbol{J}(\boldsymbol{r})$ with $\boldsymbol{r} = (x, y, z)$ in Ω be the current density distribution due to the injection current. Then, the induced magnetic flux density $\boldsymbol{B}(\boldsymbol{r})$ satisfies

$$\boldsymbol{J}(\boldsymbol{r}) = \frac{1}{\mu_0}\nabla \times \boldsymbol{B}(\boldsymbol{r}). \tag{1}$$

We first select a transversal imaging slice $\Omega_s \subset \Omega$ as shown in Fig. 1(a). Among the three components B_x, B_y, and B_z of $\boldsymbol{B}(\boldsymbol{r})$ in Ω, only B_z is in the same direction as the main magnetic field $\boldsymbol{B}_0 = B_0\boldsymbol{a}_z$ of the MRI system and is measurable since it affects the phase of the spin-echo MR image. We obtain two sets of MR images applying injection currents with opposite polarities. Then, the phase difference $\Delta\varphi(\boldsymbol{r})$ with $\boldsymbol{r} \in \Omega_s$ between these two images becomes

$$\Delta\varphi(\boldsymbol{r}) = 4\gamma B_z(\boldsymbol{r})T_D \text{ in } \Omega_s \tag{2}$$

where $\gamma = 42.6$ MHz/T is the gyromagnetic ratio of hydrogen atom and T_D is the time duration of the injection current pulse. We can produce B_z image in Ω_s due to the injection current I from (2). In this paper, an MR phase image is an image of $\Delta\varphi(\boldsymbol{r})$ and a magnetic flux density image means an image of $B_x(\boldsymbol{r})$, $B_y(\boldsymbol{r})$, or $B_z(\boldsymbol{r})$.

Now, we rotate the subject by 90° as shown in Fig. 1(b) and select three sagittal imaging slices $\Omega_{s-\Delta}$, Ω_s, and $\Omega_{s+\Delta}$ in Ω. In Fig. 1(b), $\boldsymbol{B}_0 = B_0\boldsymbol{a}_x$ due to the rotation and B_x in the three imaging slices are now measured using the same procedure described above. Note that we need three imaging slices since we compute $\partial B_x/\partial z$ and $\partial B_x/\partial y$ in (1) using the three-point difference scheme. Fig. 1(c) shows how we can measure B_y from three coronal imaging slices $\Omega_{s-\Delta}$, Ω_s, and $\Omega_{s+\Delta}$ after another 90° rotation. Once we obtain a complete set of data $\boldsymbol{B} = (B_x, B_y, B_z)$, we can compute $\boldsymbol{J}$ in Ω, from (1).

B. Geometrical Error Correction and Phase Denoising

We set up our 0.3-T experimental MREIT system with 25-cm bore shown in Fig. 2(a) to produce 128×128 MR images. Due to the main magnetic field inhomogeneity and the gradient field nonlinearity, MR images from transversal, sagittal, and coronal slices contain different amounts of geometrical distortions. Inhomogeneous susceptibility distribution inside the subject may also cause geometrical distortions. The geometrical distortion caused by the susceptibility is, however, considered to be negligibly small at the low field strength of 0.3 T. Since we must compute the internal current density at every pixel using magnetic flux density images (B_x, B_y, and B_z) of the corresponding imaging slices, we need a way to make geometrical error corrections.

Fig. 2(b) shows a three-dimensional (3-D) grid phantom ($50 \times 50 \times 50$ mm, acrylic plastic) constructed for this correction. We obtain seven (one transversal, three sagittal, and threes coronal) images of the grid phantom corresponding to the configurations shown in Fig. 1(a)–(c), respectively. Fig. 3(a)–(c) shows three (one transversal, one sagittal, and one coronal) images among them. By detecting centers of grid points on each image, we construct mapping functions $\boldsymbol{\mathcal{M}}_i$ with $i = 1, \ldots, S$ where S is the total number of imaging slices ($S = 7$ in our case). Each mapping function $\boldsymbol{\mathcal{M}}_i$ is

$$\boldsymbol{\mathcal{M}}_i(x, y) = (\tilde{x}, \tilde{y}) \text{ with } i = 1, \ldots, S \tag{3}$$

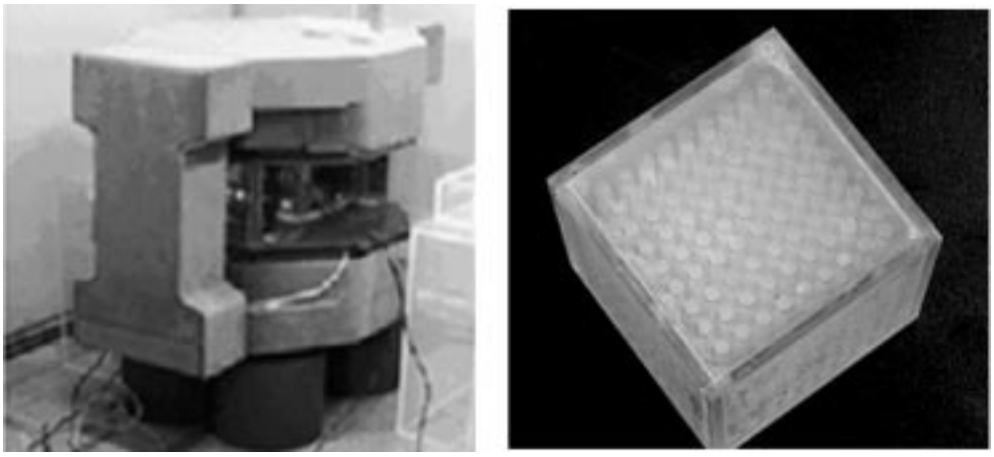

(a) (b)

Fig. 2. (a) Experimental MRI system (0.3 T) with 25-cm bore. (b) Grid phantom for geometrical error correction.

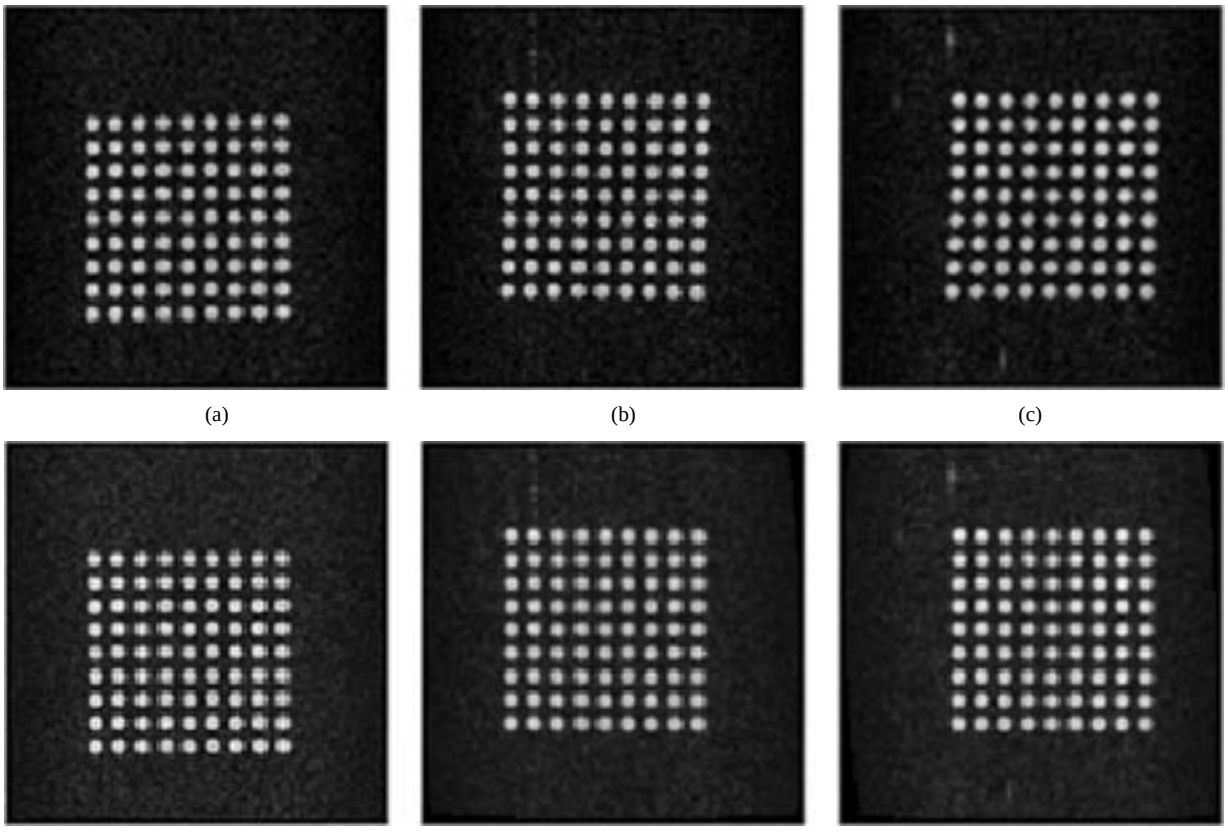

(a) (b) (c)

(d) (e) (f)

Fig. 3. (a) Transversal, (b) sagittal, and (c) coronal image of the grid phantom before geometrical error correction. (d) Transversal, (e) sagittal, and (f) coronal image of the grid phantom after geometrical error correction.

where $(\tilde{x}, \tilde{y}) \in \mathbb{R}^2$ is a point in a distorted image and $(x, y) \in \mathbb{N}^2$ is a point in the corresponding image after geometrical error correction. We assume that mapping functions $\boldsymbol{\mathcal{M}}_i$ are approximately fifth order polynomials, as

$$\begin{bmatrix} \tilde{x} \\ \tilde{y} \end{bmatrix} = \begin{bmatrix} a_0 + a_1 x + a_2 y + a_3 xy + a_4 x^2 + a_5 y^2 + \cdots + a_p y^5 \\ b_0 + b_1 x + b_2 y + b_3 xy + b_4 x^2 + b_5 y^2 + \cdots + b_p y^5 \end{bmatrix}. \quad (4)$$

Using coordinates of grid points in Fig. 3(a)–(c), we compute coefficients a_i and b_i in (4) by the least square method. Then, we correct the geometrical distortion by performing image warping with mapping functions $\boldsymbol{\mathcal{M}}_i$ and two-dimensional (2-D) linear interpolation. Fig. 3(d)–(f) shows images of the grid phantom after geometrical error corrections.

Since we plan to use the three-point difference scheme in computing $\partial/\partial x$, $\partial/\partial y$, and $\partial/\partial z$ for (1), we extract 66×66 phase images covering the inside of the subject Ω to obtain a 64×64 current density image. MR phase images due to

an injection current suffer from phase wrapping and random noise. In order to restore the continuity of phase images, we apply a simple one-dimensional phase unwrapping method since absolute phase values are made irrelevant by the subsequent differentiation. Phase unwrapping and appropriate scaling in (2) transform these phase images to magnetic flux density images. Before we differentiate noisy magnetic flux density images to compute $\boldsymbol{J}$ in (1), we need to improve the signal-to-noise ratio (SNR). In this paper, we use the high-order total variation-based denoising technique by Chan *et al.* [22]. This technique effectively removes random noise while keeping both slow and abrupt changes in magnetic flux density images. Since the SNR of our 0.3-T experimental MRI system is quite poor, this denoising process is essential.

C. Static Resistivity Image Reconstruction Algorithm: J-Substitution Algorithm

Let us assume that we inject a current I through two electrodes attached on the surface of a subject Ω with a true resistivity distribution $\boldsymbol{\rho}^*$. The induced magnetic flux density $\boldsymbol{B}^*$ in the selected imaging slice $\Omega_s \subset \Omega$ is measured by MRCDI technique described in Section II-B. In addition, we measure the voltage difference V^* between two current injection electrodes. We compute the current density $\boldsymbol{J}^*$ using (1). Then, the magnitude of $\boldsymbol{J}^*$ is

$$J^* = \sqrt{(J_x^*)^2 + (J_y^*) + (J_z^*)^2} \text{ in } \Omega_s. \tag{5}$$

The resistivity image reconstruction problem means to find a constructive map $\{I, J^*, V^*\} \rightarrow \boldsymbol{\rho}^*$ in Ω_s.

Now, we construct a finite-element model of the subject Ω with appropriate boundary conditions including electrodes and the injection current. J-substitution algorithm described in this section is iterative and we denote k as the iteration number. We take an initial guess of the true resistivity distribution $\boldsymbol{\rho}^*$ as $\boldsymbol{\rho}^k$ with $k = 0$. Given $\boldsymbol{\rho}^k$ and boundary conditions, the forward solver using FEM computes the voltage difference V^k between two electrodes and the current density $\boldsymbol{J} = \left(J_x^k, J_y^k, J_z^k\right)$ in Ω_s. Then, the magnitude of $\boldsymbol{J}^k$ is

$$J^k = \sqrt{(J_x^k)^2 + (J_y^k)^2 + (J_z^k)^2} \text{ in } \Omega_s. \tag{6}$$

Let us assume that the true resistivity in a pixel or a small region $\omega \subset \Omega_s$ is ρ_ω^* and the resistivity of the model in the corresponding region is ρ_ω^k. Here, we assume that the resistivity in ω is homogeneous and isotropic. Eventually, we want

$$J_\omega^* = \frac{1}{\rho_\omega^*} E_\omega^* = \frac{1}{\rho_\omega^k} E_\omega^k = J_\omega^k \tag{7}$$

where E is the magnitude of electric field intensity. Now let us consider two different resistivity distributions $\boldsymbol{\rho}^1$ and $\boldsymbol{\rho}^2$ for the same subject Ω with the same boundary conditions. If $\boldsymbol{\rho}^2 = \alpha\boldsymbol{\rho}^1$ where α is a positive constant, then the internal current density $\boldsymbol{J}^1$ corresponding to $\boldsymbol{\rho}^1$ is identical to $\boldsymbol{J}^2$ corresponding to $\boldsymbol{\rho}^2$ for the same injection current. However, the voltage difference between two current injection electrodes satisfies $V^2 = \alpha V^1$. Therefore, during iterations, we update ρ_ω^{k+1} as

$$\rho_\omega^{k+1} = \rho_\omega^k \frac{J_\omega^k}{J_\omega^*} \frac{V^*}{V^k}. \tag{8}$$

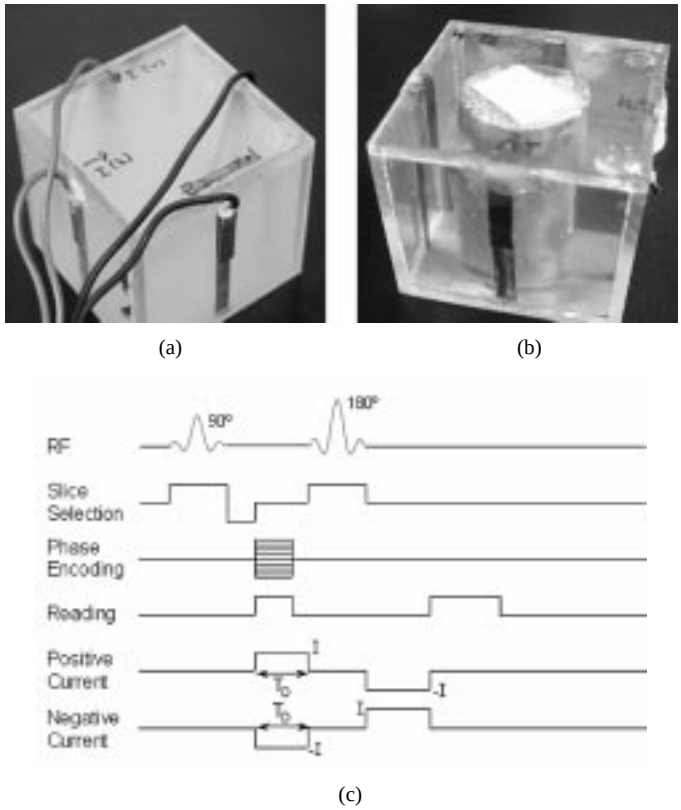

Fig. 4. Cubic saline phantoms with a dimension of $50 \times 50 \times 50$ mm: (a) homogeneous phantom and (b) phantom with a cylindrically shaped insulating object around the center. (c) Spin echo pulse sequence using two current pulses with opposite polarities.

Kwon *et al.* called this updating strategy J-substitution and described the derivation of the scheme in detail [13], [15].

Kwon *et al.* described the need for at least two different injection currents in order to guarantee the uniqueness of the reconstructed resistivity distribution [13], [15]. As they suggested, we use four electrodes uniformly spaced on the surface of the subject. Injection current I^1 is applied through two of them facing each other on vertical direction and I^2 between the other two electrodes facing each other on horizontal direction. After we compute ρ_ω^{k+1} using (8) for all $\omega \subset \Omega_s$, we increase k by one and repeat until a stopping condition is met.

D. Numerical Implementation

In this paper, we assume that the resistivity distribution in Ω does not change in z direction. For the cubic subject shown in Fig. 1, long electrodes in z direction enable us to use a 2-D finite-element model since we can safely assume $J_z = 0$. Therefore, we used a finite-element mesh including 4,225 nodes and 64×64 quadrilateral elements with each element corresponding to a pixel in the current density image from the MRCDI technique. We can change the number of nodes and elements as needed to match the spatial resolution of the current density image. We used the conjugate gradient method for sparse matrix in solving the resulting linear system of equations. After we computed all node voltages due to an injection current, we calculated the current density within each element ω as $\boldsymbol{J}_\omega = -(1/\rho_\omega)\nabla V_\omega$. We performed all computations using a PC with 1–GHz Pentium III CPU and 256-MB RAM.

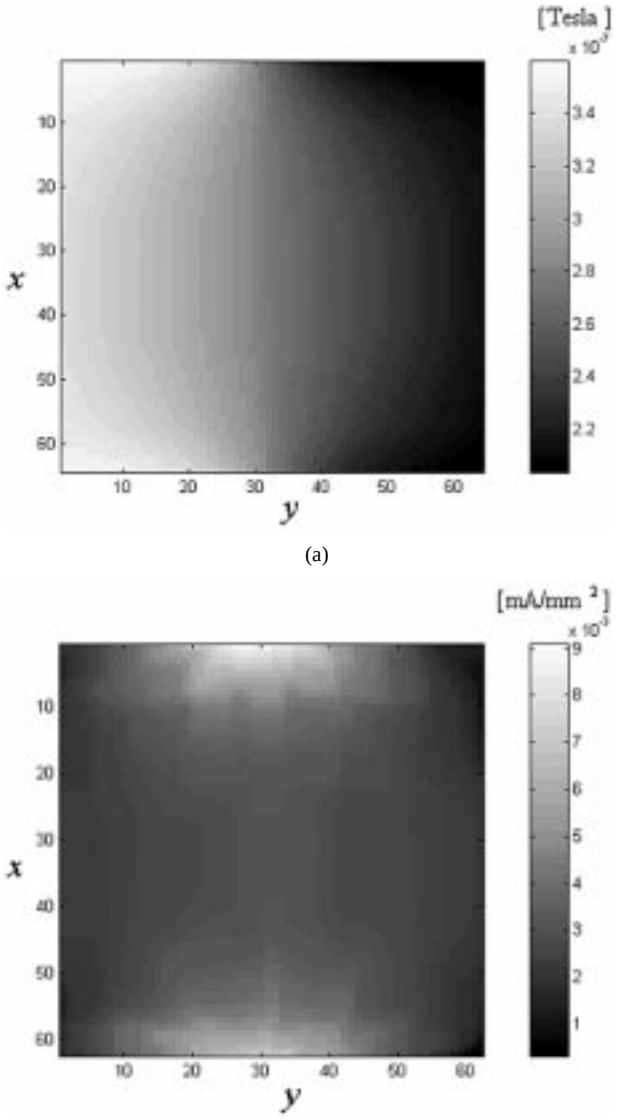

Fig. 5. (a) Magnetic flux density image of B_z from the homogeneous phantom due to injection current I^1 (vertical direction). For the homogeneous phantom, both B_x and B_y are negligible. (b) Image of the current density J^1.

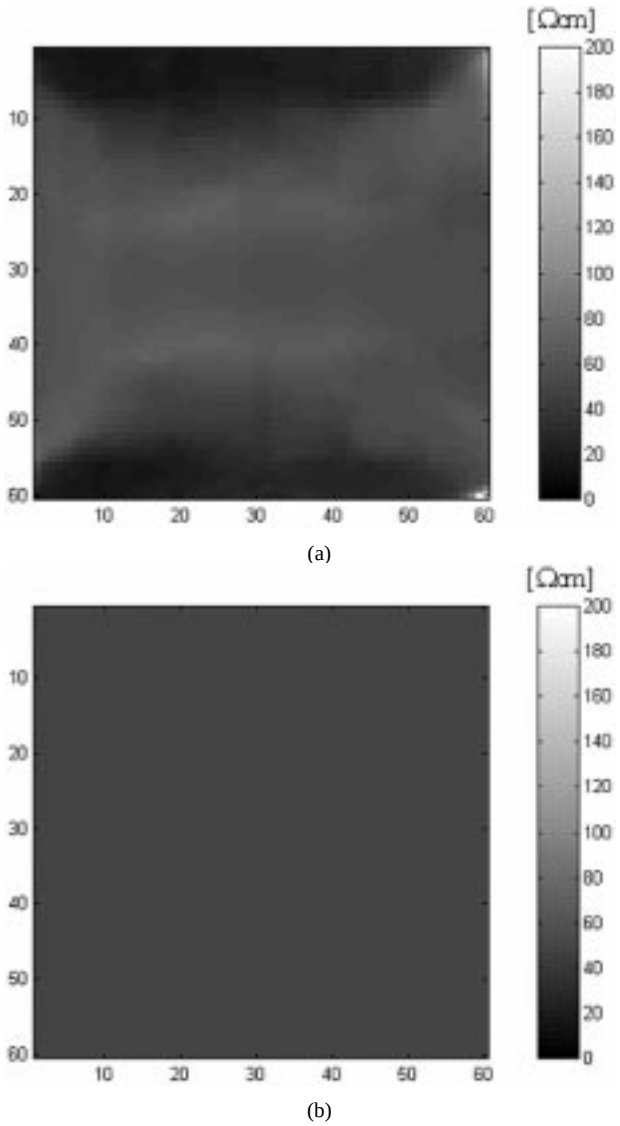

Fig. 6. (a) Reconstructed cross-sectional resistivity image of the homogeneous phantom after nine iterations of J-substitution algorithm. (b) True cross-sectional resistivity image of the homogeneous phantom.

E. Phantom Experiments

Our 0.3-T experimental MREIT system shown in Fig. 2(a) has a much lower SNR compared with other systems (at least 1.5 T and 1-m bore) used in MRCDI studies [16]–[21]. Therefore, we have to expect current density images with lower accuracy. Even though the theory of MRCDI is well established, it requires a very carefully designed experimental procedure including subject rotations and data processing methods.

Fig. 4(a) shows a homogeneous cubic phantom ($50 \times 50 \times 50$ mm, acrylic plastic) filled with a solution containing 12.5 g/l NaCl and 2 g/l $CuSO_4 \cdot 5H_2O$. The resistivity of the solution was 50 Ωcm. The phantom in Fig. 4(b) was filled with the same solution and contains an insulating object around the center. The insulating object was a cylindrically shaped potato with 30-mm diameter completely wrapped up with polyethylene sheet of 0.05 mm thickness. We checked the insulation using HP4192A Impedance Analyzer (Agilent Technologies, Co., Palo Alto, CA). The resistivity distribution of the phantom in Fig. 4(b) does not change along z direction due to the cylindrical shape of the insulating object. We used four copper electrodes with a length of 50 mm and width of 5 mm. A constant current source located outside the shield room selected a pair of electrodes for the injection current I^1. After collecting all image data for I^1, we switched it to the other electrode pair for the injection current I^2.

Two injection current pulses with a width of 48 ms and opposite polarities were synchronized with a standard spin echo pulse sequence shown in Fig. 4(c). The amount of injection current was 55 mA. The pulse repetition time was 300 ms and the echo time was 50 ms. The slice thickness was 10 mm and the field of view was about 77 mm. In obtaining 128×128 MR images, the number of averaging was eight and phase encoding step was 128. The pixel size was 0.6015×0.6015 mm^2.

III. Results

A. Homogeneous Phantom

Fig. 5(a) shows the magnetic flux density image of B_z from the homogeneous phantom in Fig. 4(a) for the injection current

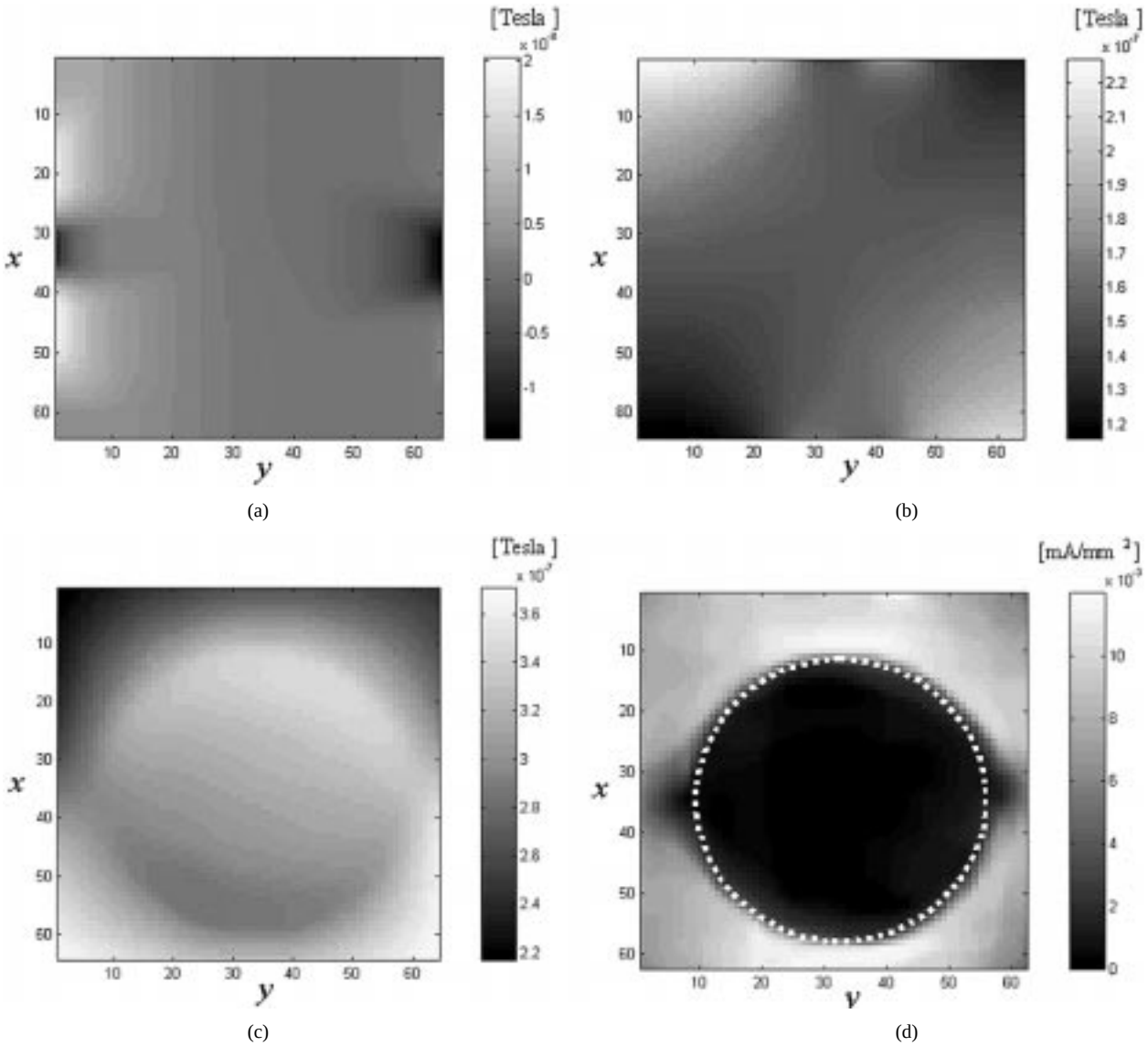

Fig. 7. Magnetic flux density images of the phantom with an insulating object around the center due to injection current I^2 (horizontal direction): (a) B_x, (b) B_y, and (c) B_z. (d) Image of the current density J^2. Current densities within the insulator are nonzero due to the noise in magnetic flux density images. Dotted circle shows the location and shape of the insulating object.

I^1 (vertical direction). It was obtained after phase unwrapping, geometrical error correction, and denoising. For the homogeneous phantom, both B_x and B_y are negligible. Fig. 5(b) shows the image of the current density J^{1^*} obtained from the magnetic flux density image. Using two current density images of J^{1^*} and J^{2^*}, we applied J-substitution algorithm with a homogeneous initial guess to reconstruct the cross-sectional resistivity image in Fig. 6(a). Fig. 6(b) shows the true cross-sectional resistivity distribution of the homogeneous phantom. In resistivity image reconstructions, we excluded the layer of about six pixels near surface of the phantom since the accuracy of the current density there is too poor. We stopped the iteration when the relative error

$$\varepsilon(k) = \frac{||\boldsymbol{\rho}^k - \boldsymbol{\rho}^{k-1}||}{||\boldsymbol{\rho}^k||} \tag{9}$$

became less than 0.01. We found that the resistivity image reconstruction does not depend on the choice of the initial guess. We also found that the error in the reconstructed resistivity values is smaller in the central region. The accuracy of the reconstructed resistivity image was 6.8% at the central region, 47.2% at the peripheral region, and 39.9% for the entire image.

B. Phantom With an Insulating Object

Fig. 7(a)–(c) shows magnetic flux density images of B_x, B_y, and B_z, respectively, from the phantom in Fig. 4(b) for the injection current I^2 (horizontal direction). Fig. 7(d) shows the image of the current density J^{2^*} obtained from magnetic flux density images. Using two current density images of J^{1^*} and J^{2^*}, we applied J-substitution algorithm with a homogeneous initial guess to reconstruct the cross-sectional resistivity image in Fig. 8(a). Fig. 8(b) shows the true cross-sectional resistivity distribution. We can clearly distinguish the insulating object from the background in Fig. 8(a). The average resistivity value of 25×25 pixels within the insulating object was 6,576.5 Ωcm compared with the background resistivity of 50 Ωcm. At some

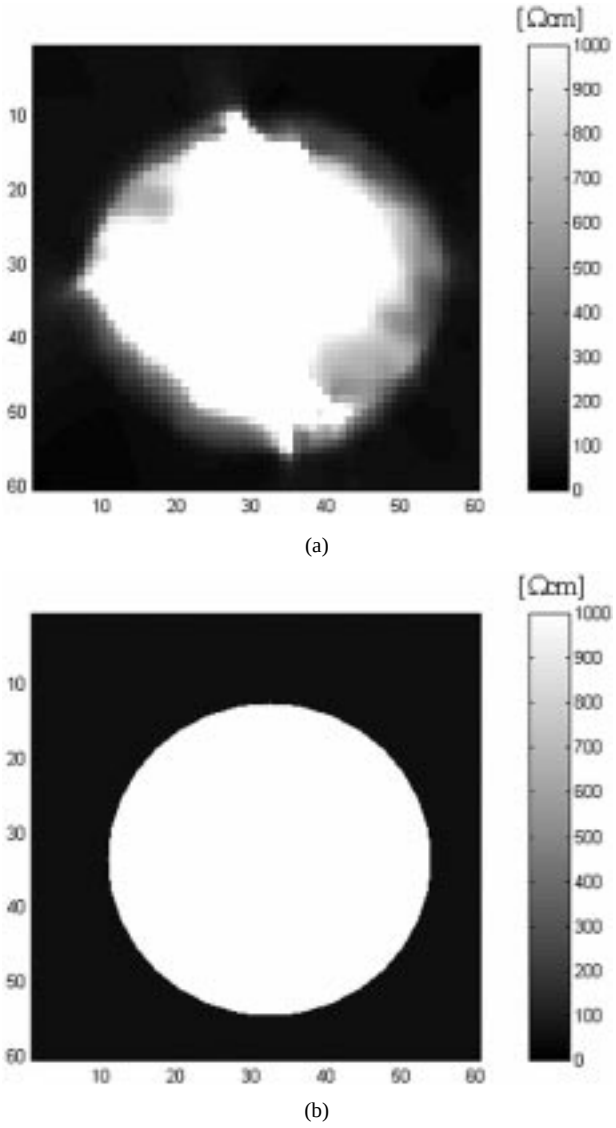

Fig. 8. (a) Reconstructed cross-sectional resistivity image of the phantom with an insulating object after nine iterations of J-substitution algorithm. (b) True cross-sectional resistivity image of the phantom with an insulating object.

pixels within the insulating object, the resistivity values were relatively low since the current densities there were greater than zero mainly due to the low SNR of less than about 15 dB in magnetic flux density images.

IV. Discussion

From the measured magnetic flux density images, we found that the accuracy is poor near electrodes compared with the central region since copper electrodes act as radio-frequency shielding layers reducing the signal amplitude around them. From a pilot study, we observed that electrodes made of silicone containing silver powder might provide better results. We need to further investigate the use of different electrode materials.

Even though we can apply the geometrical error correction and denoising technique described in this paper, it is essential to use a high-performance MRI system with better field homogeneities and SNR. We found that the poor SNR of our 0.3-T experimental MREIT system is the most important source of errors in current density images. If SNR is high enough using 1.5- or 2-T system, we will be able to improve the image quality significantly and also reduce the amount of injection current and rotation angle. However, since we cannot always completely remove the random noise in MR phase images, the denoising technique needs to be further investigated considering the physical laws of electromagnetism in biological tissues. Modified forms of the total variation-based denoising technique by Chan *et al.* [22] seem to be most promising.

In this paper, we inject currents though two facing electrodes. As Kwon *et al.* pointed out, two current patterns I^1 and I^2 used in this paper guarantee the uniqueness of the reconstructed resistivity image using J-substitution algorithm [13], [15]. However, as currents spread inside the subject, the magnitude of current density at some interior regions may be very low. Then, the magnitude of the induced magnetic flux density is also reduced producing a lower SNR. It would be worthwhile studying different current injection methods using multiple electrodes and current sources as is done in some EIT systems [1]–[9].

The resistivity image reconstruction in MREIT is essentially a 3-D problem as in conventional EIT. When the resistivity distribution considerably changes in z direction, we cannot keep using the 2-D model as adopted in this paper. In this case, we must capture magnetic flux density images on many slices along z direction and perform 3-D resistivity image reconstructions using a 3-D finite-element model. For 3-D image reconstructions, we will need to investigate the shape, size, and location of electrodes considering 3-D current flows inside the subject.

If we are only interested in resistivity images of a 2-D cross-section, we may assume that the resistivity distribution does not change much in z direction within a thin imaging slice. We define two more thin imaging slices on the top and bottom of the selected slice and collect current density images from these three slices. Then, we construct a 3-D finite-element model of the slice at the middle and use the current density data on the top and bottom slice as boundary conditions for the model. The MREIT technique described in this paper can also be applied to an internal sub-domain of the subject. Let us assume that we define a region of interest (ROI) within a certain imaging slice. At the boundary of the ROI, we use the current density data there as boundary conditions for the finite-element model of the ROI. Then, we can run resistivity image reconstructions only within the ROI.

Combining the method by Zhang [10] with J-substitution is worth more investigation. It is well known from the basic electrostatics that $V_{1,2} = \int_l \rho \boldsymbol{J} \cdot \boldsymbol{dl}$ holds where $V_{1,2}$ is the voltage difference between two electrodes 1 and 2 at the boundary and l is an interior line integral path connecting 1 and 2. First, it provides the compatibility condition for the reconstruction result using J-substitution. Second, in every iteration during image reconstruction, we can alternate J-substitution and Zhang's method using a few boundary voltage data. These boundary voltage data will supplement the internal current density data especially when the SNR of magnetic flux density images is low.

In MREIT, structural information about the subject is always available from MR magnitude images. Therefore, we can utilize this a priori information in resistivity image reconstructions

as well as boundary shape modeling. MREIT is very likely to be a multi-modality medical imaging technique providing resistivity images in addition to conventional MR images. There is also a great chance for MREIT to be very useful in functional imaging.

V. Conclusion

MREIT utilizes internal current density measurements by the MRCDI technique to overcome the inherent ill-posedness of the static EIT image reconstruction problem. Using a 0.3-T experimental MREIT system, we reconstructed static resistivity images with a spatial resolution of 64×64. The accuracy of resistivity values in the reconstructed image was estimated as 6.8% at the central region, 47.2% at the peripheral region, and 39.9% for the entire image. Even though the accuracy is quite low, this paper demonstrates the feasibility of the method. The spatial resolution and accuracy are mainly limited by the SNR in MR phase images obtained with current injection. Further improvements in both spatial resolution and accuracy will be possible using a better MRI system with a high SNR.

One of the major problems in MREIT described in this paper is the requirement of subject rotation. Even though we can reduce the rotation angle at the expense of the reduced SNR, any subject rotation in current clinical MR imaging environments seems to be very difficult. In order to make this technique more applicable to clinical situations, a new kind of MRI system allowing subject rotation needs to be developed. On the other hand, we pursue different ways of resistivity image reconstruction based only on the measurement of B_z. When we can get only B_z images without subject rotation, they still contain a lot of information on resistivity distributions. Our future study also includes image reconstructions for complicated resistivity distributions using agar phantoms and human subjects.

References

[1] *Electrical Impedance Tomography*, J. G. Webster, Ed., Adam Hilger, Bristol, UK, 1990.

[2] K. Boone, D. Barber, and B. Brown, "Imaging with electricity: Report of the european concerted action on impedance tomography," *J. Med. Eng. Tech.*, vol. 21, no. 6, pp. 201–232, 1997.

[3] T. J. Yorkey, J. G. Webster, and W. J. Tompkins, "Comparing reconstruction algorithms for electrical impedance tomography," *IEEE Trans. Biomed. Eng.*, vol. BME-34, pp. 843–852, 1987.

[4] M. Cheney, D. Isaacson, J. C. Newell, S. Simske, and J. Goble, "NOSER: An algorithm for solving the inverse conductivity problem," *Int. J. Imag. Syst. Tech.*, vol. 2, pp. 66–75, 1990.

[5] E. J. Woo, P. Hua, J. G. Webster, and W. J. Tompkins, "A robust image reconstruction algorithm and its parallel implementation in electrical impedance tomography," *IEEE Trans. Med. Imag.*, vol. 12, pp. 137–146, Apr. 1993.

[6] C. Cohen-Bacrie and R. Guardo, "Regularized reconstruction in electrical impedance tomography using a variance uniformization constraint," *IEEE Trans. Med. Imag.*, vol. 16, pp. 562–571, Oct. 1997.

[7] P. Edic, D. Isaacson, G. Saulnier, H. Jain, and J. C. Newell, "An iterative Newton–Raphson method to solve the inverse conductivity problem," *IEEE Trans. Biomed. Eng.*, vol. 45, pp. 899–908, July 1998.

[8] M. Vauhkonen, D. Vadasz, P. A. Karjalainen, E. Somersalo, and J. P. Kaipio, "Tikhonov regularization and prior information in electrical impedance tomography," *IEEE Trans. Med. Imag.*, vol. 17, pp. 285–293, Apr. 1998.

[9] A. L. Hyaric and M. K. Pidcock, "An image reconstruction algorithm for three-dimensional electrical impedance tomography," *IEEE Trans. Biomed. Eng.*, vol. 48, pp. 230–235, Feb. 2001.

[10] N. Zhang, "Electrical Impedance Tomography based on Current Density Imaging," M.S. thesis, Dept. Elec. Eng., Univ. Toronto, Toronto, ON, Canada, 1992.

[11] E. J. Woo, S. Y. Lee, and C. W. Mun, "Impedance tomography using internal current density distribution measured by nuclear magnetic resonance," *SPIE*, vol. 2299, pp. 377–385, 1994.

[12] M. Eyuboglu, O. Birgul, and Y. Z. Ider, "A dual modality system for high resolution-true conductivity imaging," in *Proc. XI Int. Conf. Elec. Bioimpedance (ICEBI)*, 2001, pp. 409–413.

[13] O. Kwon, J. K. Seo, E. J. Woo, and J. R. Yoon, "Magnetic resonance electrical impedance tomography," *Comm. Korean Math. Soc.*, vol. 16, no. 3, pp. 519–541, 2001.

[14] O. Kwon, J. K. Seo, E. J. Woo, J. R. Yoon, S. Y. Lee, and M. H. Cho, "Resistivity image reconstruction using J-substitution algorithm for MREIT," in *Proc. 23rd Ann. Int. Conf. IEEE Eng. Med. Biol. Soc.*, Istambul, Turkey, 2001.

[15] O. Kwon, E. J. Woo, J. R. Yoon, and J. K. Seo, "Magnetic resonance electrical impedance tomography (MREIT): Simulation study of J-substitution algorithm," *IEEE Trans. Biomed. Eng.*, vol. 49, no. 2, pp. 160–167, Feb. 2002.

[16] M. L. G. Joy, G. C. Scott, and R. M. Henkelman, "*In vivo* detection of applied electric currents by magnetic resonance imaging," *Mag. Reson. Imag.*, vol. 7, pp. 89–94, 1989.

[17] G. C. Scott, M. L. G. Joy, R. L. Armstrong, and R. M. Henkelman, "Measurement of nonuniform current density by magnetic resonance," *IEEE Trans. Med. Imag.*, vol. 10, pp. 362–374, Sept. 1991.

[18] ——, "Sensitivity of magnetic-resonance current density imaging," *J. Mag. Reson.*, vol. 97, pp. 235–254, 1992.

[19] H. R. Gamba and D. T. Delpy, "Measurement of electrical current density distribution within the tissues of the head by magnetic resonance imaging," *Med. Biol. Eng. Comput.*, vol. 36, pp. 165–170, 1998.

[20] M. Eyuboglu, R. Reddy, and J. S. Leigh, "Imaging electrical current density using nuclear magnetic resonance," *Elektrik*, vol. 6, no. 3, pp. 201–214, 1998.

[21] M. L. G. Joy, V. P. Lebedev, and J. S. Gati, "Imaging of current density and current pathways in rabbit brain during transcranial electrostimulation," *IEEE Trans. Biomed. Eng.*, vol. 46, pp. 1139–1149, Sept. 1999.

[22] T. Chan, A. Marquina, and P. Mulet, "High-order total variation-based image restoration," *SIAM J. Sci. Comput.*, vol. 22, no. 2, pp. 503–516, 2000.